Pt-based catalysts for NOx reduction from H2 combustion engines

Catalysis Science & Technology

ROYAL SOCIETY OF CHEMISTRY

PAPER

View Article Online
View Journal

Cite this: DOI: 10.1039/d4cy00153b

Pt-based catalysts for NO_x reduction from H_2 combustion engines†

Jieling Shao, Phuoc Hoang Ho, Wei Di, Derek Creaser and Louise Olsson *

Received 2nd February 2024,
Accepted 26th April 2024

DOI: 10.1039/d4cy00153b

rsc.li/catalysis

Platinum supported on SSZ-13 zeolite has been found to be a potential catalyst for the selective catalytic reduction of NO by H_2. This work has studied the effects of the H_2/NO molar feed ratios (0/4.4/8.8/13.2) and the impact of water on the performance of the H_2-SCR of NO on the Pt/SSZ-13 catalyst. A higher H_2/NO ratio promoted the start of the reaction at lower temperatures and favoured the production of N_2. The effect of Pt loadings was also studied with three loadings of 0.5/1.0/2.0 wt%. It was found that the 0.5 wt% Pt sample displayed the highest N_2 selectivity of 75%. In addition, an inhibiting effect of water for H_2-SCR at low temperatures was proved. Pt/SSZ-13 has shown good hydrothermal durability after 6 h in total ageing pretreatment at 800 °C and interestingly the nitrogen formation even increased. The support effect of SSZ-13, BETA and Al_2O_3 on H_2-SCR was evaluated in terms of catalytic performance and their catalytic durabilities by hydrothermal ageing experiments, showing that zeolites are significantly better for H_2 SCR. *In situ* DRIFT measurements helped to explore the mechanism of H_2-SCR on the Pt catalyst. A careful design of the measurements was used to distinguish the overlapping peaks of the water on the DRIFT spectrum. NH_4^+ ions are formed and it was shown that they play a role as intermediates during the reaction to assist the NO reduction.

Introduction

Many new energy sources are being used to replace conventional fuels in vehicles to decrease the emissions of greenhouse gases (GHG). In particular, the European Commission has published the GHG-related regulation *via* 'A European Green Deal' which targets no net emissions of greenhouse gases by 2050, which presents a significant challenge. An interesting solution is therefore to use green hydrogen as a fuel. Although the exhaust gases from H_2 internal combustion engines (ICE) are cleaner than those from diesel or gasoline engines, the formation of NO_x is unavoidable due to the oxidation of nitrogen in the air at elevated temperatures in the chamber of the ICE. In response to this issue, selective catalytic reduction (SCR) of NO_x is an essential technology to remove the NO_x emission.[1–3] Ammonia SCR under lean gas conditions is widely used as the industrial NO_x control technology since V_2O_5–WO_3/TiO_2 was commercialized for stationary applications in the 1970s.[4] Nowadays, Cu, Fe, and V-based materials are commonly used as NH_3-SCR catalysts for cleaning emissions from vehicles.[5–7] For ammonia SCR a urea system is needed to produce ammonia, however, in so-called hydrogen SCR, it would be beneficial to be able to use hydrogen directly as a reductant.

Platinum group metals, in particular Pt and Pd, have been examined for H_2-SCR catalysts due to their good water resistance.[8] Pt-based catalysts exhibit superior activity in H_2-SCR; however, they form large amounts of N_2O,[9,10] while Pd-based catalysts show better nitrogen selectivity.[11–13] A variety of materials such as oxides, different oxide combinations, perovskites, *etc.* have been used as supports for the development of H_2-SCR catalysts.[14] Costa and co-workers have studied Pt supported on various metal oxides (Al_2O_3, SiO_2, La_2O_3, MgO, Y_2O_3, CaO, CeO_2, TiO_2, and MgO–CeO_2), and found that among different catalysts, Pt/MgO and Pt/CeO_2 showed good catalytic activity and the binary oxide of 50 wt% MgO–50 wt% CeO_2 was the best.[15,16] However, the studies on zeolite as the support for H_2-SCR catalysts are more limited. Some works have reported that Pt supported on HY,[17] HZSM-5,[18,19] HMCM-41,[20] and HFER[21] zeolites were highly active for H_2-SCR due to the large surface area and the appropriate acidity, which is beneficial for the N_2 selectivity.[22] Additionally, Shibata *et al.* found that the N_2 selectivity for Pt/zeolites were generally higher than those on Pt/metal oxides and were in order of Pt/MFI > Pt/BEA > Pt/Y, Pt/MOR.[23] Yokota *et al.*[24] also reported that Pt-ZSM was more active than Pt/SiO_2 and Pt/γ-Al_2O_3. In another work, Li *et al.* found that Pt–Ti-MCM-41 exhibited good stability and tolerance against SO_2 and CO.[20]

Chemical Engineering, Competence Centre of Catalysis, Chalmers University of Technology, 412 96 Gothenburg, Sweden. E-mail: louise.olsson@chalmers.se

† Electronic supplementary information (ESI) available. See DOI: https://doi.org/10.1039/d4cy00153b

SSZ-13, a typical small-pore zeolite, is a well-known support for the development of Cu-based catalysts for NH_3-SCR applications and the Cu-SSZ-13 catalysts have superior activity and N_2 formation selectivity due to their extraordinary physiochemical properties.[25–27] In this respect, the Cu-SSZ-13 catalyst was firstly commercialized in 2010 for NO_x emission control due to its excellent performance.[28,29] It not only possesses high activity at low temperatures, but its stable hydrothermal durability can cope with realistic operations.[30,31] However, according to our knowledge, there are only limited published studies where Pt is supported on HSSZ-13 as the catalyst for H_2-SCR. Hong *et al.*[32] have reported that Pt/SSZ-13 exhibited an NO conversion of 81% at 100 °C with 91% N_2 selectivity and this catalyst was better than Pt/ZSM-5 and Pt/SAPO-34 during stability tests in the presence of SO_2 and H_2O. Their activity test was performed in a microreactor (4 mm) with a powder catalyst (20–40 mesh).

Moreover, the mechanisms of H_2-SCR on Pt-based catalysts have been examined by researchers. Costa *et al.* studied the nitrogen pathway in the reaction on Pt/MgO–CeO_2 by SSITKA-MS and SSITKA-DRIFTS, in order to identify the structure-active and inactive chemisorbed NO_x species.[33] Zhang and co-workers proposed an N_2O formation route over Pt/HY in H_2-SCR, where they suggested that the N_2O was mainly formed at the Pt–support interface with H spillover.[34] In addition, relevant studies have also reported the effect of the interaction between Pt and the support on the reaction and the effect of some additive metals, such as Na.[35,36]

However, although the H_2-SCR reaction is not a new reaction, most of the effect studies (H_2/NO ratio, O_2 concentration, water content, Pt loadings, *etc.*) deal with Pt/oxide catalysts. Studies on Pt/SSZ-13 are limited. Compared to Hong's work, the catalytic performances are evaluated here by a flow reactor with wash-coated monoliths instead of pure powder catalysts which is closer to a realistic after-treatment configuration. Moreover, the mechanism is examined here by using *in situ* DRIFT (*in situ* diffuse reflectance infrared Fourier transformed spectroscopy) spectroscopy. In addition, for the first time according to our knowledge, hydrothermal ageing is examined for Pt/SSZ-13 used for H_2-SCR. This study aims to develop Pt/SSZ-13 catalysts as efficient catalysts for NO_x reduction by H_2. The effect of H_2/NO ratios, Pt loadings, water concentrations and hydrothermal ageing have also been investigated by comparing the catalyst performance for the H_2-SCR reaction.

Experimental

Catalyst synthesis

Three different supports BETA, SSZ-13 and Al_2O_3 were compared. The test results showed that the Pt supported on zeolites (SSZ-13 or BEA) exhibited significantly more nitrogen formation compared to Pt/Al_2O_3. Since SSZ-13 is well-known to be a superior support for ammonia SCR, compared to for example BETA, considering hydrothermal stability, it was chosen for this study. The activity results for both de-greened and aged catalyst, including the preparation of the Pt/BEA and Pt/Al_2O_3 catalyst can be found in the ESI.†

SSZ-13 zeolite was prepared by hydrothermal synthesis from a gel with the following molar composition: $0.1Na_2O : 1SiO_2 : 0.025Al_2O_3 : 0.2$*N*,*N*,*N*-trimethyl-1-adamantylammonium hydroxide (TMAdOH) : $44H_2O$.[37] Sodium hydroxide (VMR Chemicals), aluminum hydroxide hydrate (Sigma-Aldrich), and fumed silica (Sigma-Aldrich) were used as sodium, aluminium, and silica sources, respectively. TMAdOH (TCI) was used as a template to help generate the Chabazite (CHA) structure. After stirring and ageing overnight, a uniform gel was formed and it was transferred to a Teflon-lined stainless-steel autoclave, heated to 160 °C and kept for 6 days. The product was washed several times with Milli-Q water and dried at 80 °C overnight. The powder was ground and calcined to remove the template at 600 °C for 8 h. The Na-SSZ-13 obtained after calcination was ion-exchanged with 0.5 M NH_4NO_3 (Thermo Scientific) solution (100 mL per 1 g powder) at 80 °C for 2 h, washed with Milli-Q water, and repeated twice. After that, the sample was dried overnight at 80 °C and calcined at 550 °C for 6 h to obtain the H-form of SSZ-13 (H-SSZ-13).

Three samples of Pt/SSZ-13 with different loadings of Pt (0.5 wt%, 1.0 wt%, 2.0 wt%) were prepared by an incipient wetness impregnation technique. Pt solution was prepared by mixing $Pt(NO_3)_4$ precursor (Alfa Aesar, 15 wt% Pt) and Milli-Q water to have a total volume similar to the wet volume of the zeolite support. The wet volume of H-SSZ-13 was approximately 0.6 mL g^{-1}, close to the total pore volume determined with N_2 physisorption measurement. The Pt solution was dropped slowly on 4 g of H-SSZ-13 zeolite placed in a mortar and after each drop, the mixture was conscientiously ground using a pestle to achieve a homogeneous distribution.[38] After impregnation, the sample was dried overnight at 80 °C and subsequently calcined at 600 °C for 8 h to obtain the powder catalyst.

The synthesized catalyst powder after calcination was then dissolved in a solution (50 wt% ethanol and 50 wt% Milli-Q water) with a 5 wt% boehmite binder (Disperal P2, Sasol) as a slurry and dip-coated onto a honeycomb monolith (cordierite, $D \times L$ = 1.5 cm × 2.0 cm, 400 cpsi) until the desired loading (300 mg) of washcoat was reached.[39] The honeycomb monolith was cut from the commercial substrate. Coated monoliths were subsequently dried in an oven at 80 °C overnight and then calcined at 500 °C for 2 h. Detailed information regarding the monolith preparation can be found elsewhere in our previous work.[40,41]

Activity measurements

Catalytic tests were performed with a laboratory-scale flow reactor (synthetic gas bench, SGB), where the monolith was inserted into a horizontal reactor tube (inner diameter: 16 mm) and wrapped in quartz wool to prevent the passage of gases around the outside of the monolith. The inlet gas mixture was regulated by Bronkhorst mass flow controllers

Table 1 The activity test procedure and reaction conditions (GHSV = 20 000 h^{-1} (STP))

Step	H_2-SCR experiment	Conditions
1	Degreening & pretreatment	(i) 10% O_2 in Ar for 4 h at 550 °C (ii) 10% O_2 and 5% H_2O in Ar for 30 min at 500 °C
2	Cooling	(i) Cooling from 500 °C to 80 °C in Ar (rate: 5 °C min^{-1}) (ii) keep at 80 °C for 30 min
3	Test cycle × 5	(i) Continuous reaction from 80 °C to 500 °C (heating rate: 5 °C min^{-1}) in the gas mixture of 500 ppm NO, varying H_2 concentration, 10% O_2, 0/5% H_2O in Ar (ii) keep at 500 °C with the same gas mixture for 20 min (iii) continuous reaction from 500 °C to 80 °C (cooling rate: 5 °C min^{-1}) in the same gas mixture

(MFCs) and water vapour was produced by a controlled evaporation and mixing system (CEM). The mole fractions of all the gases at the outlet of the reactor were measured and monitored by FTIR (MKS™ Multigas 2030) and mass spectrometry (HPR-20 QIC). The flow reactor experiments are presented in Table 1 and Fig. S1.† Firstly, the catalyst monolith was de-greened using 10 mol% O_2 in Ar balance at 550 °C for 4 h and pretreated using 10% O_2 and 5 mol% H_2O at 500 °C for 30 min with a total flow rate of 1200 NmL min^{-1}. After the pretreatment, the test cycle of heating and cooling over a temperature range of 80 to 500 °C with a temperature ramp of 5 °C min^{-1} was repeated 5 times to remove initial experimental perturbations. In a typical experiment, the gas composition of the reactivity test was 10% O_2, 5% H_2O, 500 ppm NO, and varying H_2 concentration (H_2/NO = 0, 4.4, 8.8, 10, 13.2) in Ar balance. For 1 wt% Pt-SSZ-13 catalyst, another five-cycle test in the absence of water (dry test) was also performed to study the effect of water on the activity of the catalyst. The discussion of the activity test in section: H_2-SCR activity tests was all based on the data of the 4th cycle. It should be noted that for 2 wt% Pt/SSZ-13, two different monoliths were prepared using the same batch of catalyst. The first monolith was used to study the effect of H_2/NO ratio (after multiple other cycling experiments) and the effect of hydrothermal ageing. Monolith 2 was used to compare the activity for different Pt loadings. Other experimental details can be found in the ESI.†

Catalyst characterization

Powder X-ray diffraction (XRD) measurements were conducted using a Bruker AXS D8 advance operating at 40 kV and 40 mA with Cu Kα radiation to verify the materials' crystalline structure. The samples were scanned from 2θ range of 5° to 80° with a step size of 0.02° and scan time of 1 s per step. Elemental compositions (Si, Al, Pt) of the catalysts were analyzed with inductively coupled plasma sector field mass spectrometry (ICP-SFMS) analysis which was performed by ALS Scandinavia (Luleå, Sweden). N_2 physisorption measurements were carried out at −196 °C with a Micromeritics Tristar II 3000 Analyzer. Before the measurement, around 0.1 g powder samples were degassed at 250 °C for 16 h under an N_2 atmosphere. The specific surface area was determined by the Brunauer–Emmett–Teller (BET) method in a range of relative pressure p/p_0 from 0.05 to 0.3. Additionally, the pore volume was calculated using the *t*-plot method.

CO chemisorption measurements were performed by using an ASAP2020 Plus instrument (Micromeritics). Around 0.1 g catalyst powder sample was placed in a U-shape reactor with quartz wool. Before measurement, the sample was degassed in He and underwent 1 h of H_2 reduction at 400 °C for pretreatment. After that, the powder sample was evacuated by vacuum to pressures in the range of 100–600 mmHg (at intervals of 25 mmHg) which was used for CO adsorption measurements using the double-isotherm method. The stoichiometry factor of 1 for Pt was used to calculate the amount of CO adsorption.[42,43] Combining the results of CO chemisorption and ICP, the Pt active site densities with different loadings can be calculated. The estimated active site densities with units of μmol g^{-1}, shown in Table 2, were calculated by the following equation.

$$\text{Estimated Pt site density} = \frac{W_{\text{washcoat}} \times 0.95 \times \text{Pt loading} \times \text{Dispersion} \times 10^6}{M_{\text{Pt}} \times W_{\text{washcoat}}}$$

W_{washcoat} – actual washcoat mass in the monolith
0.95 – mass fraction of actual catalyst material (other than binder) in washcoat
Pt loading – mass fraction of Pt in catalyst from ICP analysis
Dispersion – from CO chemisorption measurement
M_{Pt} – molecular weight of platinum

Table 2 Physicochemical properties of Pt/SSZ-13 de-greened catalysts with different Pt loadings

	ICP-SFMS		CO chemisorption			TEM	BET
Nominal loading of Pt/wt%	Pt/wt%	SAR (SiO_2/Al_2O_3)	Dispersion/%	Mean particle size/nm	Estimated Pt site density[a] (μmol g^{-1} washcoat)	Particle size/nm	Surface area/m^2 g^{-1}
0.5	0.51	21.6	18.6	6.1	4.53	5.4	602
1.0	1.04	21.8	11.7	9.7	5.70	7.8	616
2.0	2.04	19.4	9.9	11.4	9.64	10.1	611

[a] Estimated Pt site density = $W_{\text{washcoat}} \times 0.95 \times$ loading × dispersion/$M_{\text{Pt}}/W_{\text{washcoat}}$.

The morphology of catalyst particles was measured by transmission electron microscopy (TEM) using an FEI Titan 80-300 microscope equipped with a high-angle annular dark-field (HAADF) detector. The average particle size and distribution were calculated by random selection of over 100 particles using ImageJ software.

X-ray photoelectron spectroscopy (XPS) analysis was conducted using a PHI5000 VersaProbe III-Scanning XPS Microprobe™ with an X-ray source of monochromatic Al Kα radiation (Hv = 1486.6 eV). The system was aligned with Au (83.96 eV), Ag (368.21 eV) and Cu (932.62 eV). The measurements were calibrated with the adventitious carbon peak (C 1s) at 284.8 eV. Since the Pt $4f_{5/2}$ and Al 2p lines overlapped, we used the Pt $4f_{7/2}$ which could be observed clearly to distinguish them by the intensity ratio of Pt $4f_{7/2}$: Pt $4f_{5/2}$ = 4 : 3 and the energy separation between them is around 3.33 eV. The XPSPEAK41 software was employed for the deconvolution of experimental spectra into individual components. Background subtraction and curve fitting were processed by the Shirley model and Gauss–Lorentz functions in the software.

In situ diffuse reflectance infrared Fourier transformed spectroscopy (DRIFTS) spectra were recorded with a Bruker Vertex 70 spectrometer equipped with an MCT detector and scanning was done at 4 cm^{-1} resolution. A powder sample was placed into a sealed diffuse reflection chamber (Harrick Praying Mantis) equipped with a CaF_2 window. A mass spectrometer (Hidden HR20) was connected to the outlet to detect the out-gases. *In situ* DRIFTS was conducted for three studies. The first one is the CO adsorption on Pt-SSZ13 catalysts to determine the Pt states and thus validate the XPS results, as well as provide the estimation of the stoichiometry factor for CO chemisorption on the Pt.[44,45] The second DRIFTS study was to understand the reaction mechanism of H_2-SCR by observing different adsorbates on the surface and their changes during the adsorption of NO followed by an introduction of H_2. The last DRIFTS study aims to support the reactivity of adsorbed NH_4^+ species on the catalyst surface. Before each experiment, a pretreatment at 550 °C with 100 NmL min^{-1} of 10 vol% O_2 in Ar for 30 min was performed to clean the catalyst surface. For the CO adsorption, the background was recorded at 35 °C before the measurement. Then, a flow of 100 Nml min^{-1} containing 1000 ppm of CO/Ar was introduced to the cell for 60 min. After that CO was cut and switched to pure Ar to flush the chamber. The spectrum was recorded every minute for 63 times from introducing CO. For the H_2-SCR mechanism studies, new samples were loaded. The background was recorded at 80 °C after the pretreatment. Then, three steps were performed, firstly flowing 500 ppm NO for 60 min, flushing with Ar for 30 min, and finally introducing 5000 ppm H_2 for 60 min to investigate the reaction mechanism. To study the effect of the water spectrum, an additional measurement was performed. 5000 ppm H_2 and 5000 ppm O_2 flowed for 60 min in the system without any NO. The water formation spectrum was recorded to compare the water peaks with the peaks in the previous spectrum. Following this, the same three steps were repeated to observe the H_2-SCR reaction process. To study the different effects of the stepwise and simultaneous introduction of reacting gases, the experiment of simultaneous introduction of 500 ppm NO and 5000 ppm H_2 for 60 min was also added. Moreover, 5000 ppm O_2 was added afterwards to study the O_2 effect on the H_2-SCR reaction.

For the adsorbed NH_4^+ species reactivity study, de-greened 1 wt% Pt/SSZ-13 was loaded. In the same way as for the second study, the background was recorded at 80 °C after the pretreatment. The catalyst was first exposed to a flow of 500 ppm NH_3 for 60 min. Then Ar was purged for 60 min to remove the gas-phase NH_3 and weakly adsorbed NH_3 species. After that, 500 ppm NO was introduced and kept for 60 min. For each step, 60 spectra were recorded.

Results and discussion

Catalyst characterization

Three Pt/SSZ-13 samples with 0.5 wt%, 1.0 wt%, and 2 wt% of Pt were prepared by the incipient wetness impregnation method. The Pt loadings were determined by ICP-SFMS and they were very close to the nominal values (Table 2). The SiO_2 to Al_2O_3 molar ratio was around 20 for all samples.

The XRD patterns of the lab-synthesized H-type SSZ-13 zeolite and supported Pt catalysts with different loadings are shown in Fig. 1. The XRD pattern of H-type SSZ-13 zeolite (black curve) shows the typical reflections of chabazite (CHA) structure (by citation number: #89-0735).[46] The structure of the zeolite was, as expected, well preserved after loading with Pt. The XRD patterns of the three Pt/SSZ-13 catalysts, with different loadings, exhibited three characteristic peaks at 2θ = 39.8°, 46.2°, and 67.4° which correspond to (111), (200), and (220) reflections of bulk fcc Pt (by citation number: #04-0802),[46] respectively. These characteristic peaks of Pt in the pattern of the 0.5 wt% Pt/SSZ-13 were weak due to the low platinum content. However, the intensity of these three peaks

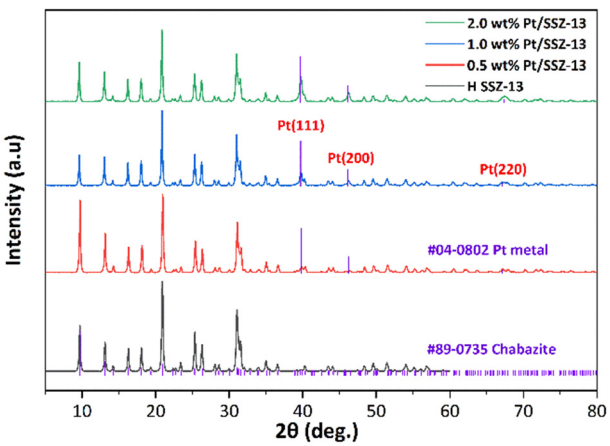

Fig. 1 X-ray diffraction patterns of H-SSZ-13 zeolite and 0.5, 1.0, and 2.0 wt% Pt/SSZ-13 catalysts.

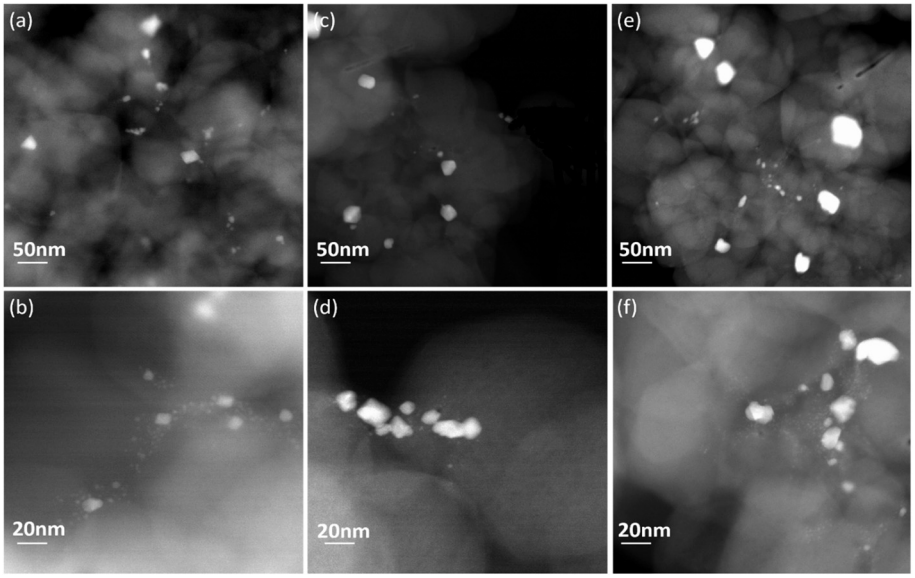

Fig. 2 HAADF-STEM images of Pt de-greened catalysts with different loadings (a and b) 0.5 wt% Pt/SSZ-13 (c and d) 1.0 wt% Pt/SSZ-13 (e and f) 2.0 wt% Pt/SSZ-13.

increased accordingly with an increase in the Pt loadings, suggesting that the crystallite size of Pt would be larger.

Nitrogen physisorption characterization revealed that the specific surface areas (S_{BET}) of the three samples are similar and in the range of 600–620 $m^2\ g^{-1}$. The Pt loadings are low and therefore do not have a great influence on the overall specific surface area.

The Pt particle sizes were determined using both STEM and CO chemisorption. The STEM images of the de-greened Pt/SSZ-13 catalysts are shown in Fig. 2 and the particle sizes determined from STEM images are shown and listed in Fig. 3 and Table 2. The average particle sizes (Fig. 3) are determined from 100 randomly selected particles in the TEM images. It should be noted that from TEM images, the observed particles have a differential distribution from small to large which lies on the external surface of zeolite. The platinum existing in ion-exchanged locations with a size smaller than the pore of zeolite (<0.4 nm) cannot be observed by TEM as well as not detected by XRD. The average particle sizes are increasing with Pt loading as expected, from 5.4 nm, 7.8 nm to 10.1 nm for 0.5, 1.0, and 2.0 wt% Pt/SSZ-13 samples. CO chemisorption measurements were performed to determine the platinum dispersion and to support the particle size determination from the TEM measurements and the results are summarized in Table 2. It should be noted that the factor of CO binding on the Pt was set as 1, based on the fact that CO was linearly adsorbed on the Pt as observed in the DRIFTS measurements (see section: *In situ* DRIFTS studies for CO adsorption). As the Pt loadings increased from 0.5 to 2.0 wt%, the dispersion of Pt particles decreased by almost half, from 18.6% to 9.9%. The mean particle sizes determined from the dispersions were 6.1 nm, 9.7 nm and 11.4 nm for 0.5, 1.0, and 2.0 wt% of Pt, respectively (Fig. 4). Noticeably, for each loading, the mean size of Pt determined by CO chemisorption was similar to the TEM measurements (Fig. 4). The particle sizes measured with TEM were slightly lower than those from CO chemisorption and this could be due to CO chemisorption being a bulk analysis technique in

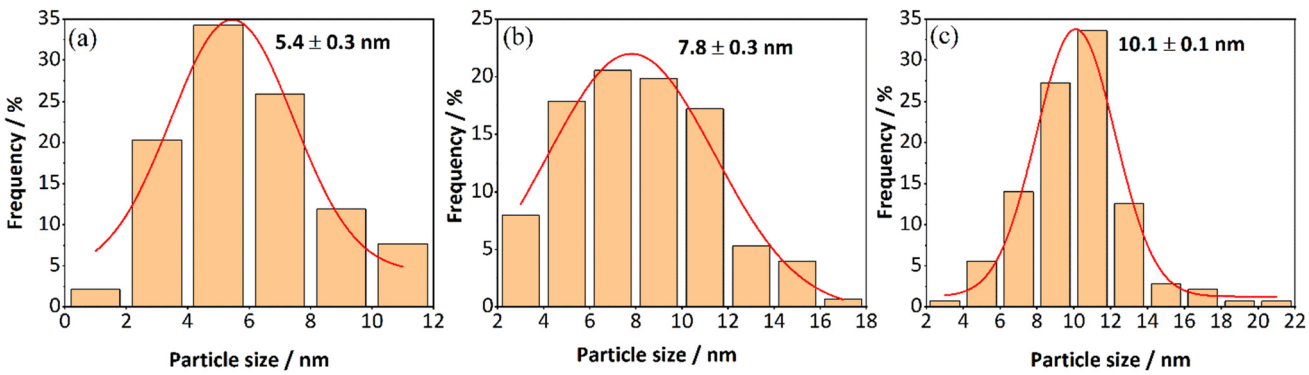

Fig. 3 Particle size distributions of Pt/SSZ-13 de-greened catalysts with (a) 0.5 wt% (b) 1.0 wt% (c) 2.0 wt% loadings.

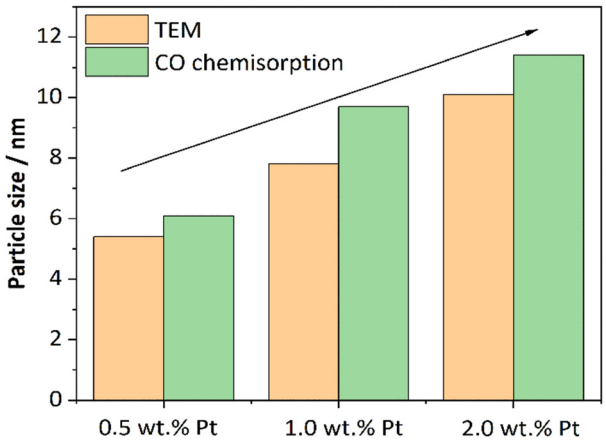

Fig. 4 Particle size trends from TEM and CO chemisorption.

which the CO probe gas can access the whole sample, whereas TEM measurements only focus on some selected areas.

The oxidation state was examined using XPS, and the results are shown in Fig. 5, where the spectra of Pt 4f core level of Pt/SSZ-13 de-greened catalysts with 1.0 wt% and 2.0 wt% Pt are compared. It should be noted that an overlap of binding energy between Al 2p and Pt 4f makes it difficult for the deconvolution of the spectrum of Pt 4f, in particular with a low loading of Pt. Therefore, we only show the data of the measurements for 1.0 wt% Pt/SSZ-13 and 2.0 wt% Pt/SSZ-13. For the specific data, the proportions of Pt states for 1.0 wt% and 2.0 wt% Pt/SSZ-13 are determined using the XPS PEAK4.1 software, and the distributions are shown in Table 3. Accordingly, the binding energy at 70.6/74.4 eV and 72.5/75.8 eV of the 1 wt% Pt de-greened sample can be assigned to $4f_{7/2}/4f_{5/2}$ of Pt^0 and Pt^{2+} species, respectively.[47,48] The peaks of the 2.0 wt% Pt de-greened sample slightly shifted the binding energies, resulting from the different interactions between Pt and zeolite caused by higher Pt loading. This is related to the net electron transfer from platinum to the support, thus changing the electron density around the metal, which has been proposed by scholars in the 1970s.[49] Interestingly, the 2.0 wt% Pt sample has a small amount of Pt^0 at 71 eV and this peak is much less intense than for the 1.0 wt% Pt/SSZ-13 samples. It is clear that the 1.0 wt% Pt sample has a larger amount of metallic Pt (73.7%) than the 2.0 wt% Pt sample (24.8%) and a lesser amount of Pt^{2+} with 26.3% compared to 75.2% for the 2.0 wt% Pt sample. Additionally, Fig. S2† was plotted to study the Pt $4d_{5/2}$ spectra due to the overlapping Al 2p peak for the Pt 4f. According to the literature,[50] the signal at the higher binding energy (316.0–317.1 eV) can be assigned to the Pt^{2+} ions, whereas the band at lower binding energy (314.3–315.5 eV) can be considered as Pt^0 species. Although the signal is weak, it can be used as an aid to demonstrate that the 1.0 wt% Pt/SSZ-13 catalyst indeed has more Pt particles in the metallic state. These results are surprising since for Pt/Al_2O_3 larger Pt particles are usually more resistant towards platinum oxidation.[51] We suggest that the reason for this surprising behaviour is that the platinum in this case is supported on a zeolite. The ion-exchanged Pt cannot be observed in our TEM images (the resolution is not high enough). Indeed, Pérez-Díaz *et al.* compared platinum supported on carbon or zeolite and found that the metallic platinum content was higher on Pt/X zeolite compared to Pt/C.[52] Simultaneously they observed that the Pt particles were larger (11.7 nm) on Pt/C than Pt/X zeolite (7.4 nm). Thus, even though the particles on Pt/X zeolite were smaller, they still were more metallic. In our case, it is the same amount of acid sites in both 1% Pt/SSZ-13 and 2% Pt/SSZ-13, which likely results in that larger fraction of the platinum in 1% Pt/SSZ-13 being ion-exchanged. Since ion-exchanged platinum results in more metallic platinum according to Pérez-Díaz *et al.*[52] this can explain why 1% Pt/SSZ-13 exhibit more metallic platinum even though the particles were smaller in TEM.

H_2-SCR activity tests

Reaction process. The activity and selectivity for H_2 SCR were studied in a flow reactor and the procedure followed a standard SCR test protocol recommended by Rappé and co-workers with some modifications.[53] The results for the fourth cycle for 2 wt% Pt/SSZ-13 are shown in Fig. 6, where NO, NO_2, and N_2O are measured with FTIR, while N_2 which

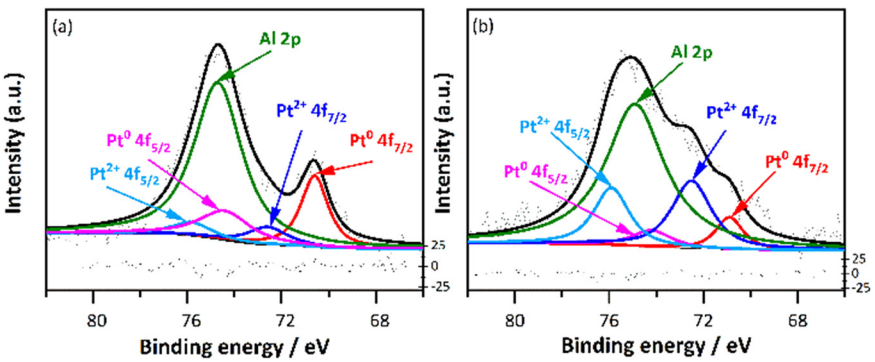

Fig. 5 X-ray photoelectron spectra of (a) 1.0 wt% Pt/SSZ-13 (b) 2.0 wt% Pt/SSZ-13 de-greened catalysts.

Table 3 Charge states of platinum in the de-greened catalysts with 1.0 wt% and 2.0 wt% Pt loadings: binding energy and fractions of the total amount

Nominal Pt loading	Pt^0		Pt^{2+}	
	BE/eV (Pt $4f_{7/2}$/Pt $4f_{5/2}$)	Fraction/%	BE/eV (Pt $4f_{7/2}$/Pt4 $f_{5/2}$)	Fraction/%
1.0	70.6/74.4	73.7	72.5/75.8	26.3
2.0	71/74.2	24.8	72.3/75.9	75.2

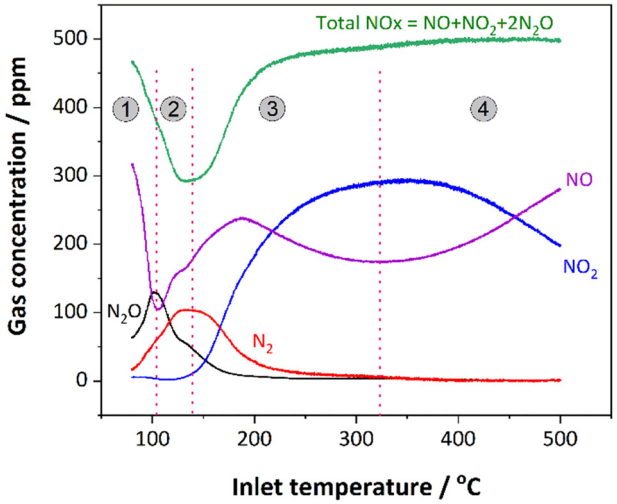

Fig. 6 NO_x and N_2 concentration of H_2-SCR reaction on 2 wt% Pt/SSZ-13 with four temperature zones ① 80–100 °C ② 100–135 °C ③ 135–330 °C ④ 330–500 °C (GHSV = 20 000 h^{-1} (STP); gas inlet: 10% O_2, 5% H_2O, 500 ppm NO, 4400 ppm H_2 balanced in Ar; *T*: 80–500 °C; heating rate: 5 °C min^{-1}).

cannot be measured with FTIR was indirectly determined based on the mass balance of nitrogen atoms. However, the presence of N_2 was confirmed by mass spectrometry of H_2-SCR on 1 wt% Pt/SSZ-13 catalyst (Fig. 10). By examining the concentration profile of NO, the reaction can be divided into four zones based on the reaction temperatures including 80–100 °C, 100–135 °C, 135–330 °C and 330–500 °C. Yang and co-workers also measured the activity performance of Pt/H-FER and showed that the NO conversion (max. 87.9%) of H_2-SCR was at a low-temperature range of 95–140 °C, and NO oxidation was occurring in the temperature range of 80–400 °C and reached a maximum at 350 °C.[54] From 80 °C to 135 °C in Fig. 6, the NO concentration decreased drastically, accompanied by a sequential increase in the concentrations of N_2O and N_2. N_2O has higher selectivity than N_2 at the first stage. NO, and H_2 first adsorb on the Pt active sites and dissociate accordingly, resulting in the formation of the product N_2 and water and by-product N_2O as well.[24] In the reaction, it has been suggested that dissociated active H spillover occurs on the catalyst surface.[55] Shin and coworkers[56] have revealed that acid sites of the zeolite play a role in initiating and facilitating H spillover based on DFT calculations. Nevertheless, H spillover requires overcoming certain energy barriers, often resulting in insufficiently active H at the Pt and support interface. When H spillover occurs from the Pt site to the support it thus produces mainly N_2O at the interface.[17] From 100 °C to 135 °C, the concentration of N_2 kept increasing to 100 ppm while N_2O decreased. It is noted that the decrement in the concentration of N_2O (black curve) is faster than that of the N_2 (red curve), showing an increased selectivity for N_2 (Fig. 6). This is because, as the main reaction progressed, the side reaction at the interface was suppressed, which could be due to the limited active H availability. In other words, the consumption of hydrogen due to hydrogen oxidation by oxygen made it insufficient for its reduction reactions. Hence, if we consider that the reactions to form N_2 and N_2O are two parallel reactions, it suggests that the reaction forming nitrogen has a higher activation energy or possibly a lower dependence on hydrogen concentration since hydrogen oxidation increases with temperature. However, as will be discussed in section: Effect of H_2/NO ratios, an increased hydrogen concentration increases the selectivity for nitrogen, thus the reaction order for hydrogen is larger for the N_2 formation reaction. Moreover, a hypothesis of a series reaction cannot be ruled out, *i.e.* the change in selectivity is due to the further reduction of N_2O to N_2 by H_2 as the temperature increases. To test this hypothesis, one additional experiment was performed with the same reaction conditions but using N_2O instead of NO. No conversion of N_2O was observed, suggesting that the sequential reduction of N_2O to N_2 by H_2 does not occur under these conditions (Fig. S3†).

Above 135 °C, the rate for oxidation of H_2 on Pt increased further and resulted in a depletion of H_2. This caused a decrease in the activity for the reduction of NO. Simultaneously, the oxidation of NO proceeded, resulting in a significant increase in NO_2 concentration. In the temperature zone of 330–500 °C, H_2 was completely consumed (Fig. S4†) since no reduction was observed, and NO was mainly oxidized to NO_2. This resulted in the absence of N_2O and N_2 in the outlet (black and red curves). Finally, at high temperatures, the NO oxidation was suppressed due to the thermodynamic equilibrium.[57]

Effect of H_2/NO ratios. The effect of different H_2/NO ratios were studied for the 2 wt% Pt/SSZ-13 catalyst and the results are shown in Fig. 7. The protocol is the standard pretreatment and continuous 20 testing cycles with H_2/NO of 0, 4.4, 8.8 and 13.2 (Table S1†). When H_2 is absent in the system, the NO was only oxidized, which started around 150 °C and reached a maximum conversion of 60% at 300 °C (black curves).[58] The conversion was decreased over 300 °C due to the thermodynamic limitation of the reaction. It can be observed from Fig. 7a that the conversion of NO has two distinct peaks after introducing 2200 ppm H_2 with NO

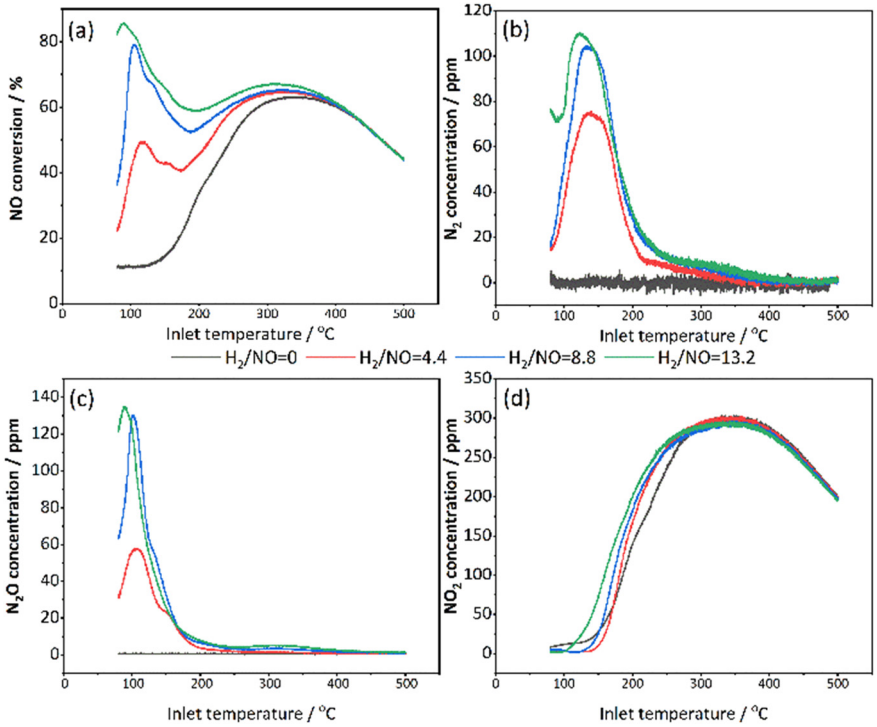

Fig. 7 Comparison of the effect of H_2/NO ratios on 2 wt% Pt/SSZ-13 catalyst, where (a) shows the conversion, and the concentration profiles are shown in (b) N_2 (c) N_2O (d) NO_2 (GHSV = 20 000 h^{-1} (STP); gas inlet: 10% O_2, 5% H_2O, 500 ppm NO, 2200/4400/6600 ppm H_2 balanced in Ar; *T*: 80–500 °C; heating rate: 5 °C min^{-1}).

reduction by H_2 at low temperature and NO oxidation at high temperature. NO reduction by H_2 produced both N_2 and N_2O in parallel reactions as discussed in section: Reaction process. As a result, the profiles of N_2 and N_2O (red curves in Fig. 7b and c) coincided with the low-temperature peak of NO conversion. At temperatures above 200 °C, H_2 was almost completely oxidized over Pt as observed with an H_2 signal measured from MS that was close to zero for the three catalysts (Fig. S7†). As a result of H_2 depletion, NO was only converted by oxidation to form NO_2 (red curve in Fig. 7d).

The conversion of NO at low and medium temperatures increased as the proportion of H_2 increased, which is consistent with the investigation by Olympiou *et al.* where Pt/MgO–CeO_2 was used for H_2 SCR.[10] They pointed out that the reduction rate of active NO_x to N_2 or N_2O will be influenced by the surface concentration of H (θ_H) on Pt, thus the N_2 selectivity as well. In Fig. 7a, the maximum NO conversion was approximately 85% for the H_2/NO ratio of 13.2, which is close to the max. NO conversion of 80% for the H_2/NO ratio of 8.8. In addition, when examining the whole temperature interval, the NO conversions were larger for the highest H_2/NO ratio. Interestingly, a small shoulder is observed in connection to the first NO conversion peak for all H_2/NO ratios. Moreover, a greater proportion of H_2 favoured the target product N_2, with a subsequent decrease in by-product N_2O (Fig. 7b and c). It is reasonable to have a higher NO reduction capacity in the presence of a larger amount of hydrogen. Both N_2 and N_2O profiles behaved with a characteristic volcano trend at low temperatures (Fig. 7b and c), but the peaks of N_2O were sharper. This means that N_2 is produced over a wider temperature range than N_2O. When the H_2 reaches 6600 ppm, most N_2 and N_2O are formed (the highest active H atom density), but it was quite similar to the condition of 4400 ppm H_2. Thus, the performance improvement is small when the H_2 concentration rises above 8.8.

NO oxidation became dominant at high temperatures (Fig. 7d). The reason is that H_2 is rapidly consumed by oxidation at high temperatures, which limited the H_2-SCR reduction. Meanwhile, an interesting phenomenon is observed from Fig. 7d that as the proportion of H_2 increased, the NO oxidation occurred earlier at lower temperatures and also the temperature for maximum NO_2 concentration shifted to lower temperatures which both indicated that the presence of H_2 promotes the NO oxidation. One of the reasons for this is an exothermic effect of the H_2 combustion during the reaction, where higher H_2 inlet concentrations resulted in higher temperatures inside the monoliths, which could further increase the reactions (Fig. S5†). It has been demonstrated and quantified in previous work by our group that the elevated monolith temperatures by hydrogen combustion promote NO oxidation.[59] In addition, the higher H_2 concentration could also result in more metallic platinum which could increase the NO oxidation.

In addition, the behaviours of H_2/NO ratios remained consistent for the 1 wt% Pt/SSZ-13 catalyst in general. The gas concentrations of NO, NO_2, N_2O and N_2 during the H_2-SCR are shown in Fig. S6.† It compared the influence of H_2

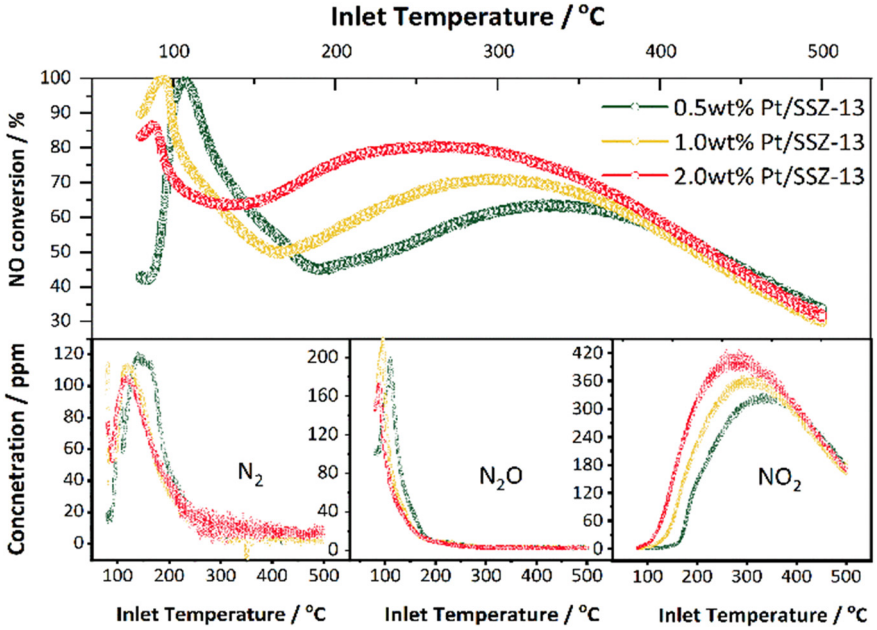

Fig. 8 Comparison of NO conversion and $N_2/N_2O/NO_2$ concentration profiles on Pt/SSZ-13 catalysts with three Pt loadings (GHSV = 20 000 h^{-1} (STP); gas inlet: 10% O_2, 5% H_2O, 500 ppm NO, 5000 ppm H_2 balanced in Ar; *T*: 80–500 °C; heating rate: 5 °C min^{-1}).

concentrations of 5000 ppm and 6600 ppm on 1 wt% Pt/SSZ-13 catalyst. The results show that the NO conversion was significantly higher on the 1 wt% Pt/SSZ-13 with a higher H_2 concentration of 6600 ppm. Moreover, under higher concentrations of H_2, the undesired by-product N_2O formation was decreased. In contrast, N_2 production was accelerated and enhanced at higher hydrogen concentrations. Additionally, on the 1 wt% Pt/SSZ-13 catalyst, H_2 continued to assist NO oxidation, with NO production occurring at lower temperatures.

Effect of Pt loadings. The effect of Pt loadings was examined, and the results are shown in Fig. 8. There are two NO conversion peaks: one is assigned to the NO reduction at lower temperatures, and the other one is assigned to NO oxidation at higher temperatures. As expected, when the Pt loading increased, the oxidation reactions were favoured which is seen by that the NO oxidation to form NO_2 increased in order from 0.5, 1 to 2 wt% Pt/SSZ-13. It also can be observed that the NO reduction reaction starts at lower temperatures with higher Pt loadings. However, the total formed N_2 and N_2O was the lowest for the 2.0 wt% Pt/SSZ-13 sample. The 2 wt% Pt sample has approximately twice the active site density compared to the 0.5 wt% Pt sample (Table 2). As a result, the H_2 is more oxidized, and less hydrogen is available for the NO reduction reactions. The outlet H_2 concentration plotted in Fig. S7† confirms this, showing that the H_2 consumption increases slower with temperature for the lower Pt loading samples, and reaches 100% consumption before approximately 100 °C. Comparing the NO_x concentration profiles of 1 wt% Pt/SSZ-13 catalyst to 2 wt% Pt/SSZ-13, slightly more N_2 and more N_2O were formed on the 1 wt% Pt/SSZ-13 catalyst. Yu *et al.*[60] have also compared the Pt loading (0.1/0.5/1.0/2.0 wt%) effects on NO reduction and oxidation over a Pt/ZSM-5 catalyst, and they found similar NO conversion profiles and the best N_2 selectivity performance on 1 wt% Pt/ZSM-35. Interestingly, in this work, it appears from the N_2 concentration profiles that N_2 was generated the most on the 0.5 wt% Pt/SSZ-13 catalyst surface. Echoing this, the selectivity profiles of the catalysts in Fig. 9 show that the N_2 selectivity was highest for the 0.5 wt% Pt/SSZ-13 catalyst, where it peaked at 167 °C. The peak N_2 selectivity decreased as the Pt loading increased.

To summarize, 0.5 wt% Pt/SSZ-13 exhibited the best catalytic performance for H_2-SCR with the highest N_2 selectivity and the total amount of nitrogen produced. Furthermore, the 2 wt% Pt/SSZ-13 sample exhibited the highest oxidation activity, but lower selectivity for the NO_x reduction reactions. This could be related to the H_2 oxidation as discussed above, but also a particle size effect, where the 0.5 wt% Pt sample has the smallest mean particle size as observed with both CO chemisorption and TEM analysis, see Fig. 3 and Table 2. A larger number of active sites gives the reactant molecules a larger reaction area and thus a higher reactivity.[61,62] However, the amount of platinum is about 4 times larger (2.04 *versus* 0.51%), while the dispersion is only doubled for the low-loaded platinum sample (18.6 *versus* 9.9%), see Table 2. This results in the 2 wt% Pt/SSZ-13 sample exhibits a factor of 2.1 times more available sites compared to the 0.5 wt% Pt/SSZ-13 sample. Olsson *et al.*[63] observed earlier that large platinum particles are more active for NO oxidation than small particles, even though there were fewer sites. These results are in line with our results where the 2 wt% Pt/SSZ-13 was very active for oxidation reactions as seen by the higher NO_2 production. This also resulted in

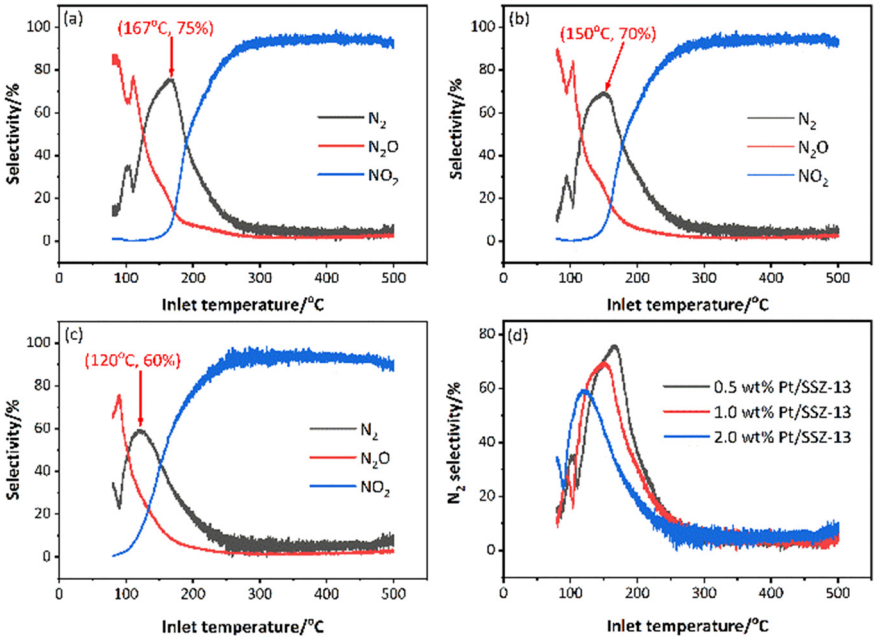

Fig. 9 Comparison of $N_2/N_2O/NO_2$ selectivity profiles on Pt/SSZ-13 catalysts with three Pt loadings (a) 0.5 wt% Pt (b) 1.0 wt% Pt (c) 2.0 wt% Pt (d) N_2 selectivities of 3 samples (GHSV = 20 000 h^{-1} (STP); gas inlet: 10% O_2, 5% H_2O, 500 ppm NO, 5000 ppm H_2 balanced in Ar; *T*: 80–500 °C; heating rate: 5 °C min^{-1}).

hydrogen being oxidized faster thereby reducing the selectivity for H_2-SCR. However, at very low temperatures, when the H_2 was not fully consumed by its oxidation, the H_2-SCR selectivity is related to the concentration of hydrogen that can reach the catalyst's active sites. In addition, the XPS results revealed (Fig. 5 and Table 3) that the lower loading sample contained a significantly larger amount of reduced platinum species, which could also be a reason for the higher selectivity for the H_2-SCR reaction.

Effect of water. The effect of water is crucial for the H_2-SCR reaction because water is the main product when combusting hydrogen and therefore it is always present in the exhaust gas stream. The catalytic behaviours were evaluated in the presence and absence of water. Fig. 10 shows the NO_x ($NO/NO_2/N_2O$) concentration profiles which were detected by FTIR during the fourth cycle of the experiment. The mass spectrometer results are included to compare the N_2 profiles under the conditions with and without water. It is clear that at low temperatures, water had a significant inhibiting effect on the reaction, which likely is due to the competitive adsorption between water molecules and NO on the active sites,[64,65] so less N_2 was produced (green curve). The inhibition effect by water was the largest at low temperatures because the water molecules desorb at higher temperatures. In the absence of water, there is more overall conversion of NO (black curve) and less production of N_2O at low temperatures which also means the selectivity of N_2 is higher. The maximum N_2O formation peak in the absence of water (blue curve) reached 100 ppm which was much less than the 212 ppm N_2O peak in the presence of water. It can be also observed that the NO_2 formation in the presence of water was less than in the absence of water, which also indicates that the presence of water inhibits the activity of the Pt centre, both for the NO reduction and for its oxidation. The negative effect of water has also been investigated by Auvray *et al.* on Pt/Al_2O_3 catalysts for NO oxidation which is consistent with this study.[66]

Hydrothermal durability. Fig. 11 reflects the hydrothermal durability of Pt/SSZ-13 catalysts. It compares the catalytic performance of degreened Pt/SSZ-13 (from Fig. 7, note that

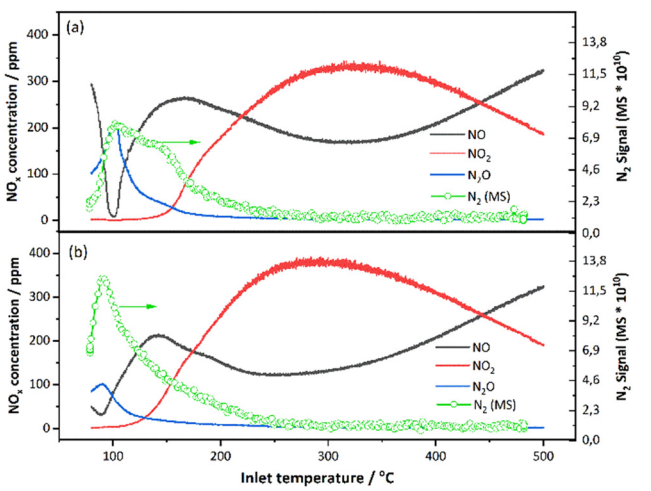

Fig. 10 Comparison of $NO/NO_2/N_2$ concentration from FITR and N_2 Signal from MS of 1 wt% Pt/SSZ-13 catalyst (a) with H_2O and (b) without H_2O (GHSV = 20 000 h^{-1} (STP); gas inlet: 10% O_2, 0%/5% H_2O, 500 ppm NO, 5000 ppm H_2 balanced in Ar; *T*: 80–500 °C; heating rate: 5 °C min^{-1}).

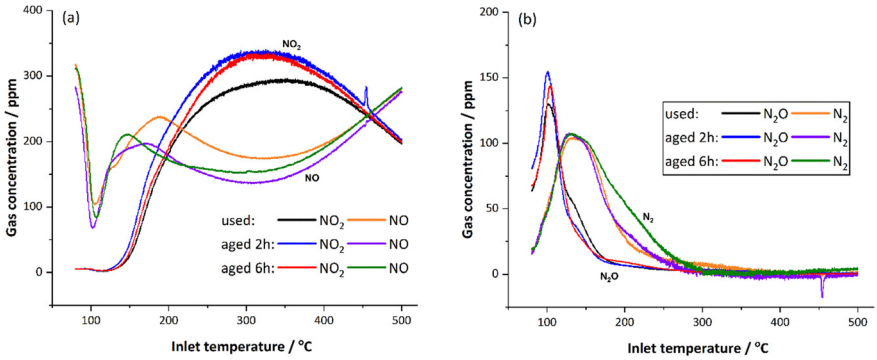

Fig. 11 (a) NO, NO_2, (b) N_2O, and N_2 concentrations of H_2-SCR on 2 wt% Pt/SSZ-13 (used from Fig. 7) and its hydrothermal pretreated for 2 h and 6 (2 + 4) h samples (GHSV = 20 000 h^{-1} (STP); gas inlet: 10% O_2, 5% H_2O, 500 ppm NO, 4400 ppm H_2 balanced in Ar; *T*: 80–500 °C; heating rate: 5 °C min^{-1}).

the sample was used for multiple cycles before these tests) and hydrothermally aged for 2 h and 6 h (2 + 4) samples. The detailed hydrothermal pretreatment procedure can be found in ESI.† The target product N_2 maintained the same amount at 107 ppm after 6 h of ageing. Interestingly, the N_2 production was slightly higher at higher temperatures (dark green line). After a total of 6 hours of deep hydrothermal ageing, there was only a slight decrease in performance compared to ageing for 2 hours, *e.g.* NO conversion, N_2O and NO_2 production. However, both aged samples (2 and 6 h) had an enhanced activity compared to the degreened sample, specifically in the conversion of NO and the generation of NO_2. NO oxidation is a structure-sensitive reaction and it is well known that larger Pt particles give larger NO oxidation.[63] In addition, it is possible that some of the PtO_x was reduced to its metallic state under hydrothermal treatment at a temperature of 800 °C, which is accompanied by particle growth and sintering.[67] In summary, Fig. 11 certainly shows a strong hydrothermal stability for Pt/SSZ-13 zeolite. In addition, as mentioned in the Experimental section also Pt/BETA and Pt/Al_2O_3 were compared under hydrothermal conditions, see Fig. S8 and S9.† Both zeolite supports (BEA and SSZ-13) were superior compared to Al_2O_3. Since SSZ-13 is a common stable support for automotive catalysis, it was the focus of the current work.

***In situ* DRIFTS studies for CO adsorption.** The Pt state with increasing loading of both fresh and de-greened samples (Fig. S10† and 12) was investigated by examining the last cycle of CO adsorption DRIFTS spectra. The peaks at 2098 cm^{-1} and 2152 cm^{-1} were attributed to CO linearly adsorbed onto metallic Pt surfaces and CO adsorbed on Pt ions – oxidic Pt species, respectively.[68–70] It should be noted that the CO gas phase bands were also in this region,[71] however, the last spectrum was recorded after cutting off CO to ensure the interference of the CO gas phase was minimized. For the peak at around 2139 cm^{-1}, Stakheev *et al.* interpreted that (i) this peak could be assigned to the CO adsorbed on the Pt sites with high coordination numbers; (ii) the possible reoxidation of Pt metal particles by zeolite protons and (iii) CO adsorption on partially reduced Pt ions.[72] Since XPS showed that some of the platinum was oxidized we assign the peak at 2139 cm^{-1} in this work to CO adsorption on partially reduced Pt ions.[72] The intensity of the peak for CO adsorbed on oxidic Pt increased with increasing Pt loading, while the intensity of the peak for CO adsorbed on metallic Pt changed with the opposite trend. The combination of the XPS and CO adsorption DRIFT spectra suggests that as the Pt loading rises, the portion of oxidized Pt species increases, with the 0.5 wt% Pt/SSZ-13 sample containing the greatest proportion of metallic Pt.

Compared to Fig. S10,† the CO-adsorption profile on the fresh samples presents some differences in trend. For the higher Pt loadings, the degreening pretreatment results in more ionic Pt, which is evident by that the peak at 2098 cm^{-1} is declining. For Cu/SAPO-34 (also chabazite structure) similar behaviour has been seen where higher temperature results in Cu migration to ion-exchanged sites that increase the activity which could be one of the reasons to explain this result.[73]

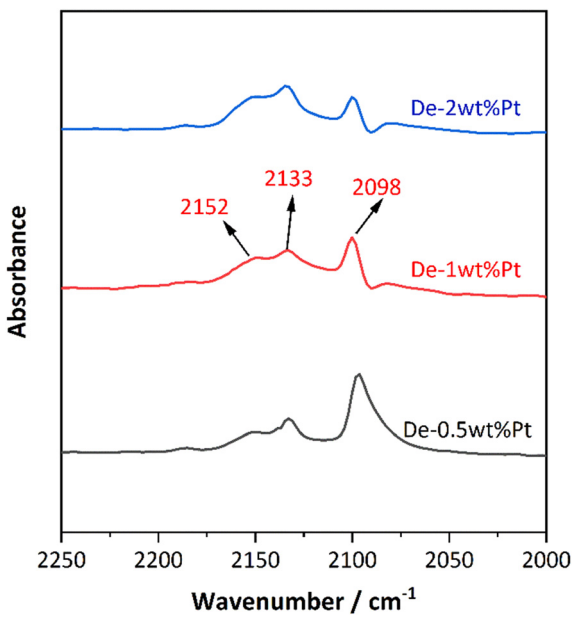

Fig. 12 CO DRIFTS spectra performed on 0.5 wt%/1.0 wt%/2.0 wt% de-greened Pt/SSZ-13 catalysts.

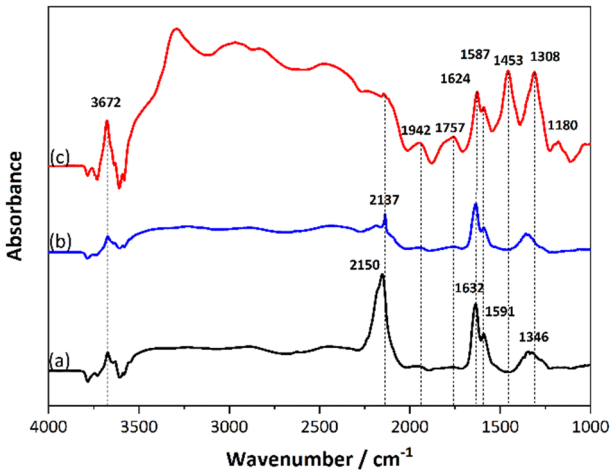

Fig. 13 *In situ* DRIFTS spectra for exposure of 1 wt% Pt/SSZ-13 under (a) 500 ppm NO at 80 °C for 60 min (b) cut NO for 60 min (c) feed 5000 ppm H_2 for 60 min.

***In situ* DRIFTS studies for NO reduction by H_2.** In order to elucidate the reaction mechanism, DRIFTS spectra were examined with 1 wt% Pt/SSZ-13 catalyst to identify the chemical structure of surface reaction intermediates after adding NO and H_2. Fig. 13 shows DRIFTS spectra of NO adsorption on the catalyst surface, NO desorption from the surface and H_2–NO reduction on the surface. After flowing NO for 60 min, the bands at 2150, 1632, 1591 and 1346 cm^{-1} were observed. It is noted that when stopping the flow of NO gas, the peaks all decreased, especially the band at 2150 cm^{-1} obviously decreased and shifted to 2137 cm^{-1} which is attributed to the desorption of nitrosyls (NO_x) species weakly adsorbed on the acidic sites of the zeolite.[74] Adsorbed nitrosyl (NO^+) co-adsorbed with a nitrate NO_3^- species on adjacent metal cation – oxygen anion site-pairs of the support for the band at 2220 cm^{-1} were also reported in the literature.[33] Notably, this band can be easily removed even at ambient-temperature evacuation which might be the reason for the peak decrease in Fig. 13b. The band recorded at 1632 cm^{-1} is assigned to the nitrates adsorbed on the Pt. These nitrates contain mainly bidentate (bridged) nitrates, but monodentate nitrates also possibly exist which were identified as active reaction intermediates at low temperatures and became inactive over 300 °C according to Savva *et al.*[74] According to the literature, the bands at 1591 cm^{-1} and 1346 cm^{-1} can be generally assigned to the nitrates and nitrito on the support.[74]

After introducing H_2 at 80 °C, new peaks at 1180, 1308, 1453, 1757 and 1942 cm^{-1} appeared. Large peaks appeared above 2000 cm^{-1} after introducing H_2 and were mainly assigned to O–H stretching from water formation. The bands at 2470 cm^{-1} and 2945 cm^{-1} referred to the OH^- and $O^{\cdot-}$ anions from water. Noticeably, a distinctive peak at 3303 cm^{-1} is shown, which can be assigned to the O–H stretching vibration of water molecules that are hydrogen bonded to the anion.[75] In the range of 3580–3800 cm^{-1}, the peaks from lower binding energies to higher binding energies are attributed to Si–OH(nest) (3590 cm^{-1}), framework bridged hydroxyl groups-AlOHSi (3630 cm^{-1}), extra framework AlOH groups (3670 cm^{-1}) and terminal silanol groups – SiOHs (3750 cm^{-1}) which are related to the OH bonds with the zeolite support.[76] Moreover, it was reported that peaks belonging to the water bending mode in the gas phase and liquid phases are located at 1594 cm^{-1} and 1642 cm^{-1} on the Al_2O_3 surface, respectively.[77] And from an FTIR study of water adsorption on H-ZSM-5 zeolite by Jobic and co-workers,[78] it was verified that the peak at 1340 cm^{-1} could belong to bridging OH groups with deformations by different zeolite structure and composition.

Since the overlap of NO adsorption and water adsorption on the surface increased the complexity of the spectra, additional measurements were performed for verification, where only H_2 and O_2 were added to the system without any NO (Fig. 13a). With only H_2 and O_2, similar peaks as appearing in the Fig. 13c were seen, which demonstrates that the peaks belonging to the water adsorption mostly covered the peaks from NO reduction. Interestingly, a band at 1453 cm^{-1} was observed in Fig. 13c that could be attributed to NH_4^+ ions, which could be one of the intermediates of the H_2-SCR reaction.[79–81] After $H_2 + O_2$ reaction there is a peak at 1465 cm^{-1} that came from the H_2O adsorption which is quite close to the peak at 1453 cm^{-1}, which might result in partial overlaps. Moreover, according to the literature,[82] peaks at 1332 cm^{-1} and 1625 cm^{-1} can be assigned to the symmetric and antisymmetric bending modes of the hydroxonium ion in the zeolite. When only flowing NO in the system (Fig. 14b), it is obvious that several peaks originally belonging to water adsorption show negative peaks due to the water removal from the surface, which also includes the peak at 1465 cm^{-1}. For the enlarged view of the region near 1633 cm^{-1} in Fig. 14b, it was been mentioned in relation to Fig. 13 that the peaks at 1633 cm^{-1} and 1591 cm^{-1} are assigned to the nitrates adsorbed on the Pt and zeolite surface respectively. The intensity of these peaks became progressively stronger as the time of NO exposure increased from 10 min to 60 min. After introducing H_2, it was observed that only the peak at 1633 cm^{-1} decreased and shifted to a lower wavenumber of 1626 cm^{-1} (dashed line), which illustrates that H_2 adsorbed on the Pt active site, attacks the nitrates on the Pt, leading to weakened binding and a changed surface intermediate structure. The peaks above 2000 cm^{-1} appeared again indicating that the H_2-SCR reaction began to occur, and water was formed. Most importantly, a new peak at 1454 cm^{-1} was formed with H_2-SCR, further suggesting the presence of ammonium ions in the reaction process. It should be noted that water also has a band at 1465 cm^{-1} (Fig. 14a) thus it is likely that the band at 1454 cm^{-1} is an overlap between ammonia and water on the surface. NH_3 has been reported as a by-product of H_2-SCR in many publications,[54,83] however the activity test in our study (section: Reaction process) did not reveal the presence of ammonia. Instead, through DRIFTS the presence of ammonium ions is shown, suggesting that the Pt/SSZ-13

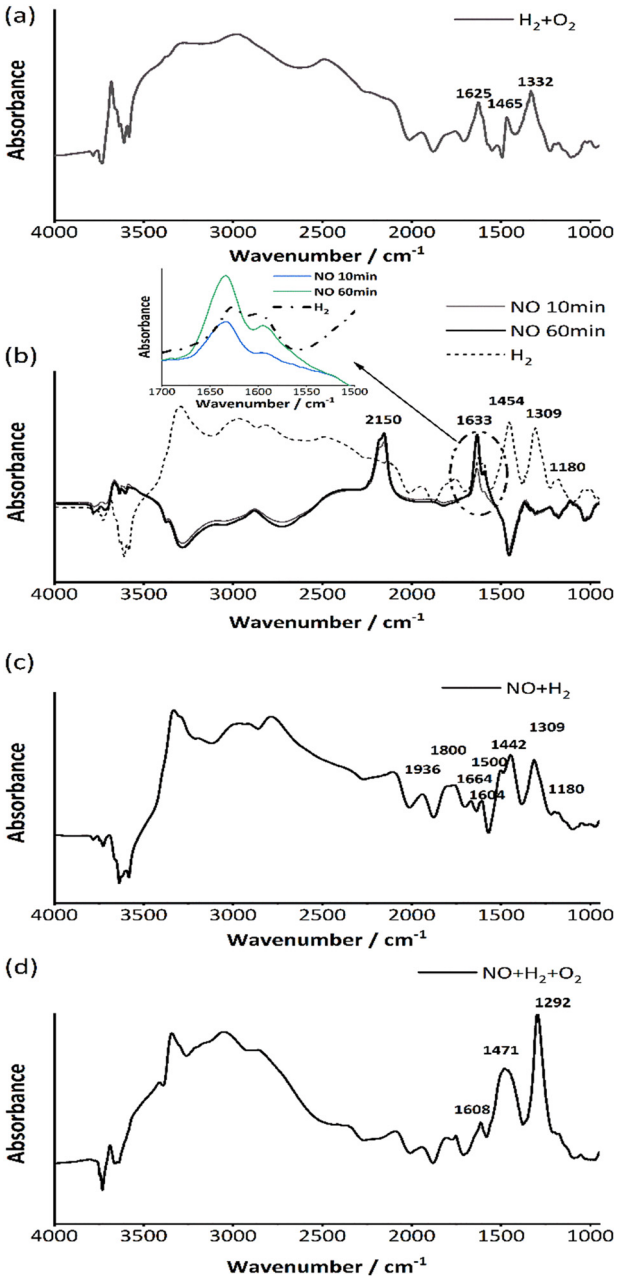

Fig. 14 *In situ* DRIFTS spectra for exposure of 1 wt% Pt/SSZ-13 at 80 °C under (a) 5000 ppm H_2 + 5000 ppm O_2 for 60 min (b) 500 ppm NO for 60 min; flush Ar for 30 min; 5000 ppm H_2 for 60 min (enlarged view of the peaks near 1633 cm^{-1}) (c) 500 ppm NO + 5000 ppm H_2 at for 60 min (d) 500 ppm NO + 5000 ppm H_2 + 5000 ppm O_2 for 60 min.

could store NH_4^+. This is in line with the study by Giordanino *et al.* who studied the interaction of NH_3 with Cu-SSZ-13,[84] and here NH_4^+ could play a role as an intermediate that assists the NO reduction. As well as the work from Shibata *et al.*, the reactions between intermediate NH_x species and NO were shown as an important pathway during the H_2-SCR process.[23] The band recorded at 1309 cm^{-1} is considered a water peak in this spectrum. Although it has been reported that it may belong to nitrites (NO_2^-) adsorbed on the support[74] due to its high peak intensity and the absence of NO flow, it is presumed to belong to water produced by the reaction. A small peak at 1180 cm^{-1} appears in all the spectra which also is assigned to OH groups.[78]

If NO and H_2 are added simultaneously (Fig. 14c), the overall spectrum is similar to Fig. 14b. However, it could be noticed that the peak at 1454 cm^{-1} was split into two peaks at 1442 cm^{-1} and 1500 cm^{-1}, respectively. The peak at 1442 cm^{-1} is considered to be a shift by the H_2 influence from the original peak at 1454 cm^{-1} of ammonium ions since the shape and intensity are quite similar.[85] Due to the reaction occurring more rapidly and the competitive adsorption of H_2 against NO_x, the small side peak at 1500 cm^{-1} is assigned to different NO_x adsorption species such as Pt_2NO.[86] Moreover, the NO_x adsorption peak in the region of 1591–1633 cm^{-1} subsequently disappeared, which could be explained by the rapid reaction in the presence of H_2. Comparing Fig. 14d with NO + O_2 + H_2, the peak at 1309 cm^{-1} is shifted to 1292 cm^{-1} with an extremely enhanced intensity and sharpness. The peak at 1309 cm^{-1} was assigned to water instead of nitrites (NO_2^-) with only H_2 feed, but here with NO + O_2 + H_2, it is reasonable to consider that nitrites also contribute to the peak. Although the peaks at 1442 cm^{-1} and 1500 cm^{-1} merged into a peak around 1471 cm^{-1} again, this peak shape is broader, and this could be due to the overlap of multiple peaks.

***In situ* DRIFTS studies for adsorbed NH_4^+ species reactivity.** To further verify the suggested mechanism relating to the surface adsorbed NH_4^+ ions as reaction intermediate facilitating the reduction of NO, additional experiments were performed. In Fig. 15a, the results from ammonia adsorption on 1 wt% Pt/SSZ-13 at 80 °C is shown. A clear peak at 1454 cm^{-1} is observed and is assigned to NH_4^+ species, consistent with the results in Fig. 13 and 14. Thereafter, the NH_3 gas is

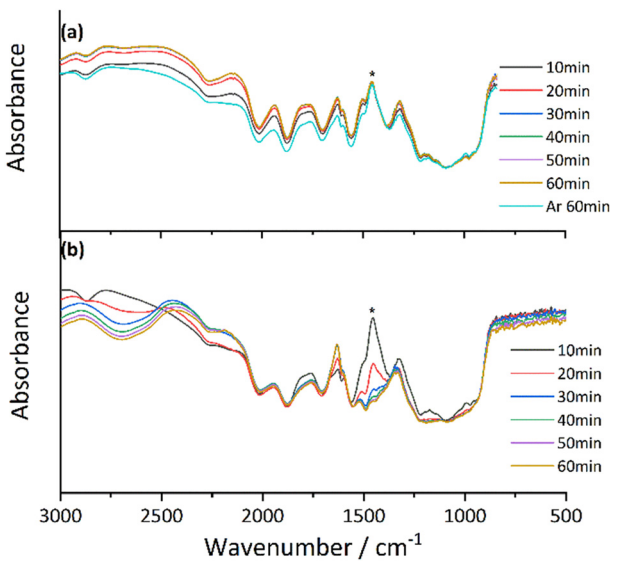

Fig. 15 *In situ* DRIFTS spectra for exposure of 1 wt% Pt/SSZ-13 at 80 °C under (a) 500 ppm NH_3 flowing for 60 min; Ar flowing for 60 min (b) 500 ppm NO flowing for 60 min.

removed for 60 min (Ar only), and the peak corresponding to NH_4^+ species at 1454 cm^{-1} retained its shape and intensity, showing stability on the surface. The subsequent introduction of NO induced a noticeable depletion of ammonium ions on the surface, especially within the first 30 min as shown in Fig. 15b. Confirmation of N_2 formation upon the introduction of NO was provided by mass spectrometry (Fig. S11†). Shibata *et al.*[23] similarly demonstrated the storage of NH_4^+ on the Brønsted-acid site of acidic supports, enhancing selective N_2 formation *via* a well-established NH_3-SCR mechanism.

DRIFTS measurements have led to a more in-depth study and understanding of the key surface intermediate species involved in the reaction. Multiple tests were carried out to reduce the complexity of the system caused by the influence of water. To sum up, i) nitrosyl species weakly adsorbed on the acidic sites of the zeolite can be easily removed. ii) H_2 absorbed on Pt was activated to interact with NO which was also absorbed on the Pt surface. iii) The formation of NH_4^+ ions was demonstrated and they can play a role as a reaction intermediate to assist in the reduction of NO, which also was shown. iv) The reaction occurred rapidly when NO and H_2 entered simultaneously, where the NO storage form was changed. v) The addition of O_2 to NO + H_2 mixture generates more nitrite (NO_2^-) species on the catalyst.

Conclusions

Pt-based, lab-synthesized SSZ-13 zeolite catalysts were prepared by an incipient impregnation method with three loadings of 0.5 wt%, 1.0 wt% and 2 wt% and characterized and activity-tested in a flow reactor with wash-coated monoliths. The reaction process is complex, with H_2-SCR mainly occurring at lower temperatures, and NO oxidation at higher temperatures, but with several side reactions. A higher proportion of H_2 with H_2/NO ratios of 4.4/8.8/13.2 promoted the reaction to start at a lower temperature and favoured the N_2 formation. Compared to the higher Pt loadings, the 0.5 wt% sample has good activity and higher maximum N_2 selectivity of 75%, this could be due to a lower oxidation of H_2 by oxygen and the fact that the catalyst contains a higher proportion of platinum in the metallic state. Water has an inhibition effect on H_2-SCR at lower temperatures due to the competitive adsorption between water and reactant molecules. Pt/SSZ-13 catalyst has shown good hydrothermal durability after 6 h in total hydrothermal ageing.

In situ DRIFT studies were done to explore the reaction mechanisms. When H_2 was introduced to an NO-saturated sample at 80 °C, water formation was observed showing that the SCR reaction was started. H_2 is absorbed on the surface of Pt active sites and is activated to interact with nitrates that are also absorbed on the Pt surface. The bonding of nitrates on the Pt was weakened. Meanwhile, NH_4^+ ions were formed and shown that during the reaction they played a role as reaction intermediates to assist in the reduction of NO. Simultaneous entry of NO and H_2 induces a faster reaction than sequential entry and affects the binding of surface species, especially NO. The introduction of O_2 to the NO + H_2 mixture generates more nitrite (NO_2^-) species on the catalyst.

Conflicts of interest

There are no conflicts to declare.

Acknowledgements

This study has been funded by Swedish Energy Agency and carried out in collaboration with Volvo AB, Scania CV and Johnson Matthey *via* a strategic vehicle research and innovation (FFI) project (P51458-1). We also appreciate the assistance for material characterizations of Dr Stefan Gustafsson (TEM measurements), Dr Eric Tam (XPS analysis), and Dr Andreas Schaefer (CO chemisorption). As well as Lennart Norberg and Lasse Urholm (Flow-reactor technical support).

Notes and references

1 J. Wang, H. Zhao, G. Haller and Y. Li, *Appl. Catal., B*, 2017, **202**, 346–354.
2 W. Shan and H. Song, *Catal. Sci. Technol.*, 2015, **5**, 4280–4288.
3 P. Granger and V. I. Parvulescu, *Chem. Rev.*, 2011, **111**, 3155–3207.
4 F. Nakajima, *Catal. Today*, 1991, **10**, 1–20.
5 D. Damma, P. R. Ettireddy, B. M. Reddy and P. G. Smirniotis, *Catalysts*, 2019, **9**(4), 349.
6 I. Nova and E. Tronconi, *Fundamental and Applied Catalysis Urea-SCR Technology for deNO$_x$ After Treatment of Diesel Exhausts*, Springer, New York, 2014.
7 H. Xue, G. Li, P. Liu, F. Wang, Y. Bai and K. Wang, *Adv. Mater. Res.*, 2012, **550**, 119–123.
8 Z. Hu and R. T. Yang, *Ind. Eng. Chem. Res.*, 2019, **58**, 10140–10153.
9 J. Shibata, M. Hashimoto, K. I. Shimizu, H. Yoshida, T. Hattori and A. Satsuma, *J. Phys. Chem. B*, 2004, **108**, 18327–18335.
10 G. G. Olympiou and A. M. Efstathiou, *Chem. Eng. J.*, 2011, **170**, 424–432.
11 L. Wang, H. Chen, M. H. Yuan, S. Rivillon, E. H. Klingenberg, J. X. Li and R. T. Yang, *Appl. Catal., B*, 2014, **152–153**, 162–171.
12 J. Li, G. Wu, N. Guan and L. Li, *Catal. Commun.*, 2012, **24**, 38–43.
13 M. Mihet, M. D. Lazar, V. Almasan and V. Mirel, *AIP Conf. Proc.*, 2012, **1425**, 73–76.
14 X. Li, X. Zhang, Y. Xu, Y. Liu and X. Wang, *Chin. J. Catal.*, 2015, **36**, 197–203.
15 C. N. Costa and A. M. Efstathiou, *J. Phys. Chem. C*, 2007, **111**, 3010–3020.
16 C. N. Costa and A. M. Efstathiou, *Appl. Catal., B*, 2007, **72**, 240–252.
17 X. Zhang, X. Wang, X. Zhao, Y. Xu, H. Gao and F. Zhang, *Chem. Eng. J.*, 2014, **252**, 288–297.

18 Z. Hong, Z. Wang, D. Chen, Q. Sun and X. Li, *Appl. Surf. Sci.*, 2018, **440**, 1037–1046.
19 Q. Yu, M. Richter, F. Kong, L. Li, G. Wu and N. Guan, *Catal. Today*, 2010, **158**, 452–458.
20 L. Li, P. Wu, Q. Yu, G. Wu and N. Guan, *Appl. Catal., B*, 2010, **94**, 254–262.
21 S. Yang, X. Wang, W. Chu, Z. Song and S. Zhao, *Appl. Catal., B*, 2011, **107**, 380–385.
22 A. Satsuma, M. Hashimoto, J. Shibata, H. Yoshida and T. Hattori, *Chem. Commun.*, 2003, 1698–1699.
23 J. Shibata, M. Hashimoto, K. I. Shimizu, H. Yoshida, T. Hattori and A. Satsuma, *J. Phys. Chem. B*, 2004, **108**, 18327–18335.
24 K. Yokota, M. Fukui and T. Tanaka, *Appl. Surf. Sci.*, 1997, **121**, 273–277.
25 F. Gao and J. Szanyi, *Appl. Catal., A*, 2018, **560**, 185–194.
26 A. M. Beale, F. Gao, I. Lezcano-Gonzalez, C. H. F. Peden and J. Szanyi, *Chem. Soc. Rev.*, 2015, **44**, 7371–7405.
27 E. Borfecchia, P. Beato, S. Svelle, U. Olsbye, C. Lamberti and S. Bordiga, *Chem. Soc. Rev.*, 2018, **47**, 8097–8133.
28 A. M. Beale, F. Gao, I. Lezcano-Gonzalez, C. H. F. Peden and J. Szanyi, *Chem. Soc. Rev.*, 2015, **44**, 7371–7405.
29 W. Hu, T. Selleri, F. Gramigni, E. Fenes, K. R. Rout, S. Liu, I. Nova, D. Chen, X. Gao and E. Tronconi, *Angew. Chem., Int. Ed.*, 2021, **60**, 7197–7204.
30 I. A. Pankin, A. Martini, K. A. Lomachenko, A. V. Soldatov, S. Bordiga and E. Borfecchia, *Catal. Today*, 2020, **345**, 125–135.
31 H. Y. Chen, Z. Wei, M. Kollar, F. Gao, Y. Wang, J. Szanyi and C. H. F. Peden, *J. Catal.*, 2015, **329**, 490–498.
32 Z. Hong, X. Sun, Z. Wang, G. Zhao, X. Li and Z. Zhu, *Catal. Sci. Technol.*, 2019, **9**, 3994–4001.
33 C. N. Costa and A. M. Efstathiou, *J. Phys. Chem. C*, 2007, **111**, 3010–3020.
34 X. Zhang, X. Wang, X. Zhao, Y. Xu, H. Gao and F. Zhang, *Chem. Eng. J.*, 2014, **252**, 288–297.
35 Z. Liu, B. Jia, Y. Zhang and M. Haneda, *Ind. Eng. Chem. Res.*, 2020, **59**, 13916–13922.
36 M. Machida and T. Watanabe, *Appl. Catal., B*, 2004, **52**, 281–286.
37 Z. Li, M. T. Navarro, J. Martínez-Triguero, J. Yu and A. Corma, *Catal. Sci. Technol.*, 2016, **6**, 5856–5863.
38 P. H. Ho, D. Yao, D. Creaser and L. Olsson, *ACS Eng. Au*, 2022, **2**, 219–235.
39 K. Wijayanti, S. Andonova, A. Kumar, J. Li, K. Kamasamudram, N. W. Currier, A. Yezerets and L. Olsson, *Appl. Catal., B*, 2015, **166–167**, 568–579.
40 P. H. Ho, J. Shao, D. Yao, R. F. Ilmasani, M. A. Salam, D. Creaser and L. Olsson, *J. Environ. Chem. Eng.*, 2022, **10**, 108217.
41 D. Yao, R. Feizie Ilmasani, J. C. Wurzenberger, T. Glatz, J. Han, A. Wang, D. Creaser and L. Olsson, *Chem. Eng. J.*, 2021, **428**, 132459.
42 G. J. Freel, *J. Catal.*, 1972, **25**, 149–160.
43 A. D. Allian, K. Takanabe, K. L. Fujdala, X. Hao, T. J. Truex, J. Cai, C. Buda, M. Neurock and E. Iglesia, *J. Am. Chem. Soc.*, 2011, **133**, 4498–4517.
44 E. Ivanova, M. Mihaylov, F. Thibault-Starzyk, M. Daturi and K. Hadjiivanov, *J. Mol. Catal. A: Chem.*, 2007, **274**, 179–184.
45 G. J. Freel, *J. Catal.*, 1972, **25**, 149–160.
46 S. Gates-Rector and T. Blanton, *Powder Diffr.*, 2019, **34**, 352–360.
47 P. Bera, K. R. Priolkar, A. Gayen, P. R. Sarode, M. S. Hegde, S. Emura, R. Kumashiro, V. Jayaram and G. N. Subbanna, *Chem. Mater.*, 2003, **15**, 2049–2060.
48 H. H. Liu, Y. Wang, A. P. Jia, S. Y. Wang, M. F. Luo and J. Q. Lu, *Appl. Surf. Sci.*, 2014, **314**, 725–734.
49 J. C. Vedrine, M. Dufaux, C. Naccache and B. Imelik, *J. Chem. Soc., Faraday Trans. 1*, 1978, **74**, 440–449.
50 K. Yang, L. Zhu, J. Zhang, X. Huo, W. Lai, Y. Lian and W. Fang, *Catalysts*, 2018, **8**, 307.
51 X. Auvray, T. Pingel, E. Olsson and L. Olsson, *Appl. Catal., B*, 2013, **129**, 517–527.
52 P. J. Pérez-Díaz, A. Medina-Ramírez, I. R. Galindo Esquivel, G. García Ruiz and B. Ruiz-Camacho, *Ionics*, 2021, **27**, 1813–1828.
53 K. G. Rappé, C. DiMaggio, J. A. Pihl, J. R. Theis, S. H. Oh, G. B. Fisher, J. Parks, V. G. Easterling, M. Yang, M. L. Stewart and K. C. Howden, *Emiss. Control Sci. Technol.*, 2019, **5**, 183–214.
54 S. Yang, X. Wang, W. Chu, Z. Song and S. Zhao, *Appl. Catal., B*, 2011, **107**, 380–385.
55 W. C. Conner and J. L. Falconer, *Chem. Rev.*, 1995, **95**, 759–788.
56 H. Shin, M. Choi and H. Kim, *Phys. Chem. Chem. Phys.*, 2016, **18**, 7035–7041.
57 L. Olsson, B. Westerberg, H. Persson, E. Fridell, M. Skoglundh and B. Andersson, *J. Phys. Chem. B*, 1999, **103**, 10433–10439.
58 L. Olsson, B. Westerberg, H. Persson, E. Fridell, M. Skoglundh and B. Andersson, *J. Phys. Chem. B*, 1999, **103**, 10433–10439.
59 M. M. Azis, X. Auvray, L. Olsson and D. Creaser, *Appl. Catal., B*, 2015, **179**, 542–550.
60 Q. Yu, M. Richter, F. Kong, L. Li, G. Wu and N. Guan, *Catal. Today*, 2010, **158**, 452–458.
61 V. V. Pushkarev, K. An, S. Alayoglu, S. K. Beaumont and G. A. Somorjai, *J. Catal.*, 2012, **292**, 64–72.
62 L. Cao, Q. Wang and J. Yang, *J. Environ. Chem. Eng.*, 2020, **8**, 103631.
63 L. Olsson, *J. Catal.*, 2002, **210**, 340–353.
64 Z. Liu, J. Li and J. Hao, *Chem. Eng. J.*, 2010, **165**, 420–425.
65 R. Burch and M. D. Coleman, *Appl. Catal., B*, 1999, **23**, 115–121.
66 X. Auvray and L. Olsson, *Appl. Catal., B*, 2015, **168–169**, 342–352.
67 E. Ogel, M. Casapu, D. E. Doronkin, R. Popescu, H. Störmer, C. Mechler, G. Marzun, S. Barcikowski, M. Türk and J. D. Grunwaldt, *J. Phys. Chem. C*, 2019, **123**, 5433–5446.
68 H. Bischofb, N. I. Jaeger, G. Schulz-Eklofp and L. Kubelkovab, *J. Mol. Catal. A: Chem.*, 1993, **80**, 95–103.
69 E. V. Benvenutti, L. Franken, C. C. Moro and C. U. Davanzo, *Langmuir*, 1999, **15**, 8140–8146.

70 Z. Zhang, Y. Zhu, H. Asakura, B. Zhang, J. Zhang, M. Zhou, Y. Han, T. Tanaka, A. Wang, T. Zhang and N. Yan, *Nat. Commun.*, 2017, **8**, 16100.
71 F. Azzolina-Jury and F. Thibault-Starzyk, *Top. Catal.*, 2017, **60**, 1709–1721.
72 A. Y. Stakheev, E. S. Shpiro, O. P. Tkachenko, N. I. Jaeger and G. Schulz-Ekloff, *J. Catal.*, 1997, **169**, 382–388.
73 C. Niu, X. Shi, F. Liu, K. Liu, L. Xie, Y. You and H. He, *Chem. Eng. J.*, 2016, **294**, 254–263.
74 P. G. Savva and A. M. Efstathiou, *J. Catal.*, 2008, **257**, 324–333.
75 J. Lengyel, M. Ončák, A. Herburger, C. Van Der Linde and M. K. Beyer, *Phys. Chem. Chem. Phys.*, 2017, **19**, 25346–25351.
76 F. Jin and Y. Li, *Catal. Today*, 2009, **145**, 101–107.
77 H. A. Al-Abadleh and V. H. Grassian, *Langmuir*, 2003, **19**, 341–347.
78 H. Jobic, A. Tuel, M. Krossner and J. Sauer, *J. Phys. Chem.*, 1996, **100**, 19545–19550.
79 Y. Shi, X. Wang, L. Chen, S. Li, C. Wu, S. Shan and W. Li, *Appl. Surf. Sci.*, 2020, **506**, 144715.
80 G. Novell-Leruth, A. Valcárcel, A. Clotet, J. M. Ricart and J. Pérez-Ramírez, *J. Phys. Chem. B*, 2005, **109**, 18061–18069.
81 S. Elzey, A. Mubayi, S. C. Larsen and V. H. Grassian, *J. Mol. Catal. A: Chem.*, 2008, **285**, 48–57.
82 H. Jobic, M. Czjzek and R. A. van Santen, *J. Phys. Chem.*, 1992, **96**, 1540–1542.
83 M. Borchers, P. Lott and O. Deutschmann, *Top. Catal.*, 2023, **66**, 973–984.
84 F. Giordanino, E. Borfecchia, K. A. Lomachenko, A. Lazzarini, G. Agostini, E. Gallo, A. V. Soldatov, P. Beato, S. Bordiga and C. Lamberti, *J. Phys. Chem. Lett.*, 2014, **5**, 1552–1559.
85 F. Giordanino, E. Borfecchia, K. A. Lomachenko, A. Lazzarini, G. Agostini, E. Gallo, A. V. Soldatov, P. Beato, S. Bordiga and C. Lamberti, *J. Phys. Chem. Lett.*, 2014, **5**, 1552–1559.
86 A. Citra and L. Andrews, *J. Phys. Chem. A*, 2000, **104**, 8160–8172.